Unconventional Anomalous Hall Effect in the Canted Antiferromagnetic Half-Heusler Compound DyPtBi

Jie Chen, Hang Li, Bei Ding, Peng Chen, Tengyu Guo, Xing Xu, Dongfeng Zheng, Hongwei Zhang, Xuekui Xi, and Wenhong Wang*

The interplay between magnetism and the topological band in metamagnetic materials has attracted researchers' attentions because these materials exhibit novel phenomena, such as the anomalous Hall effect (AHE) and quantum AHE. Here, the magnetotransport of DyPtBi single crystals in out-of-plane and in-of-plane magnetic field configurations is investigated. The results show a large unconventional anomalous Hall signal in the canted Type II antiferromagnetic state, indicating the existence of significant Berry curvature. This signal evolves into a large hump with DyPtBi entering the paramagnetic state and persists up to temperatures that are much higher than T_N. Out-of-plane and in-of-plane measurements indicate that a larger unconventional Hall signal is observed at certain θ and ϕ angles. A giant planar anomalous Hall angle (AHA) of up to 30% is achieved in DyPtBi, which is comparable to that in a typical ferromagnetic Weyl semimetal. The results show that DyPtBi is a good platform for investigating the unconventional AHE and other novel physical properties in various potentially topologically nontrivial phases due to the interplay between canted antiferromagnetic structures and topology.

1. Introduction

Magnetic topological materials with broken time-reversal symmetry, including Weyl semimetals and topological insulators, stand out as the best platforms to study unique anomalous transport phenomena based on the net Berry curvature, such as the intrinsic anomalous Hall effect (AHE), quantum AHE, and anomalous Nernst effect.[1,1a,2] In these materials, the interplay between magnetism and the nontrivial topology is an important topic because a variety of magnetic ordering textures may induce multiple topological phases.[3] This can also be an effective method of tuning the topological properties. Magnetic materials with metamagnetic transitions exhibit a variety of magnetic structures under an external magnetic field. Combined with the topological band, this offers a unique opportunity to study the nontrivial interplay between topological properties and spin textures in one material, and the coupling of conduction electrons and spins can be finely controlled by an external magnetic field of a few Teslas. Because the magnetization direction and symmetry of the spin textures in metamagnetic transition can be easily changed by an external magnetic field, the band of magnetic materials based on the symmetry and spin texture will be correspondingly tuned.[4] The interplay of magnetism and the topological band produces plentiful novel topological quantum phenomena, such as the AHE.[5] For example, in the $MnBi_2Te_4$,[3a,6] $EuCd_2As_2$,[5a,7] and $EuTiO_3$[5e] compound the metamagnetic transitions modulate the topological band and induced the nonmonotonic AHE. Research on Co_2MnAl and MnSi provides a detailed theoretical analysis on the tunable effect of symmetry of magnetic structures, demonstrating that it is an effective path to tune the topological properties.[2e,4] Magnetic topological materials with metamagnetic transitions exhibit great prospects in topological physics and the unconventional AHE.

Half-Heusler compounds are a great family, and more than 50 compounds were predicted to be topological materials.[8] Except for nonmagnetic compounds, the introduction of magnetic rare earth element R makes RPt/PdBi compounds to magnetic topological semimetals with an antiferromagnetic (AFM) ground state. Under a magnetic field, RPtBi compounds were identified to be magnetic-field-induced Weyl semimetals.[9] The Berry curvature-related nonlinear AHE was studied.[9a,10] Unlike other half-Heusler compounds, DyPtBi shows complex metamagnetic transitions under an external magnetic field and exhibits two kinds of canted AFM structures.[10c,11] Based on the fact that DyPtBi is a topological semimetal candidate,[12] this feature indicates that it can be a rare case to study the topological properties induced by the magneto-band-structure effect of the metamagnetic transition on the topological band.

J. Chen, P. Chen, T. Guo, X. Xu, D. Zheng, W. Wang
Songshan Lake Materials Laboratory
Dongguan, Guangdong 523808, China
E-mail: wenhong.wang@iphy.ac.cn
J. Chen, H. Li, B. Ding, H. Zhang, X. Xi, W. Wang
State Key Laboratory for Magnetism
Beijing National Laboratory for Condensed Matter Physics and Institute of Physics
Chinese Academy of Sciences
Beijing 100190, China

2107526 (1 of 8)

In this paper, we systematically research the magnetoelectrical transport properties of DyPtBi single crystals. The large negative longitudinal magnetoresistance (MR) implies the chiral anomaly and Weyl semimetal state of DyPtBi. Interestingly, a significant nonlinear anomalous Hall signal is observed when the magnetic field B approaches the direction parallel to the current I in the canted AFM phase. The magnetic-field dependence of the AHE indicates that the canted AFM phase is a key factor to observe the AHE and that the structure of the canted AFM phase has a large influence on tuning the AHE. The temperature dependence of the unconventional Hall signal evolves and persists to $T > T_N$. This indicates that the unconventional Hall signal at $T > T_N$ has the same origin as that at $T < T_N$. The measurement of B out of and in current plane (111) shows a strong anisotropy. In particular, the measurements of the planar AHE show a strong dependence on the crystal axis with a $2\pi/3$ period in (111) plane. The large anomalous Hall angle (AHA) reaches to 30%. The results will motivate further researches on metamagnetic topological materials and corresponding tunable topological properties.

2. Results

2.1. Metamagnetic Transition and Phase Diagram

As seen in the left inset of **Figure 1**a, the half-Heusler compound DyPtBi crystallized in a cubic structure with space group F-43m.[13] The orientation of the single crystal was determined by X-ray diffraction (XRD). The two peaks, (111) and (222), in Figure 1a, correspond to the (111) plane of the single crystal.

The typical (111) plane usually shows a triangular or hexagonal shape, as shown in the right inset. The resistivity $\rho_{xx}(0\,T)$ and magnetization M at 2–90 K are shown in Figure 1b. The temperature dependence of the magnetization with $B\,//\,[111]$ and $B = 0.05$ T shows an AFM transition at 3.5 K, which is consistent with previous results.[10c,11,13] The abrupt jump in $\rho_{xx}(0\,T)$ around T_N from 4.7 to 32.7 mΩ cm, an order of magnitude, suggests strong coupling between conduction electrons and the magnetic ordering. Similar to other magnetic RPtBi materials, DyPtBi exhibits an AFM ground state. Figure 1c displays the magnetic field (B) dependence of the magnetization (M) in DyPtBi single crystal with $B\,//\,[1\text{-}10]$ and $T = 2$ K, which reveals two step-like metamagnetic transitions at $B_{c1} = 1.3$ T and $B_{c2} = 3.1$ T. Neutron diffraction studies indicate that DyPtBi exhibits three kinds of spin texture, type II, canted type I, and canted type II with increasing B along [1-10] directions.[10c] The insets of Figure 1c show the AFM component of the spin structures, type II in region I ($0 < B < B_{c1}$), canted type I in region II ($B_{c1} < B < B_{c2}$), and canted type II in region III ($B_{c2} < B$). The ferromagnetic components are dependent on the external magnetic field. The magnetic phase diagram of the magnetic field and temperature extracted from the isothermal magnetization is exhibited in Figure 1d. This metamagnetic transition is usually observed in systems with unstable magnetic structures. However, the materials with both a metamagnetic transition and topological properties are rare. Only a few of systems have these characteristics, such as the magnetic topological insulator $MnBi_xTe_y$,[3a,14] magnetic semimetal $EuCd_2As_2$[5a,7a] and $EuTiO_3$.[5e] In topological materials, by breaking certain crystalline symmetries, topological states can be switched among several topological phases, like Weyl semimetals (WSMs), Dirac
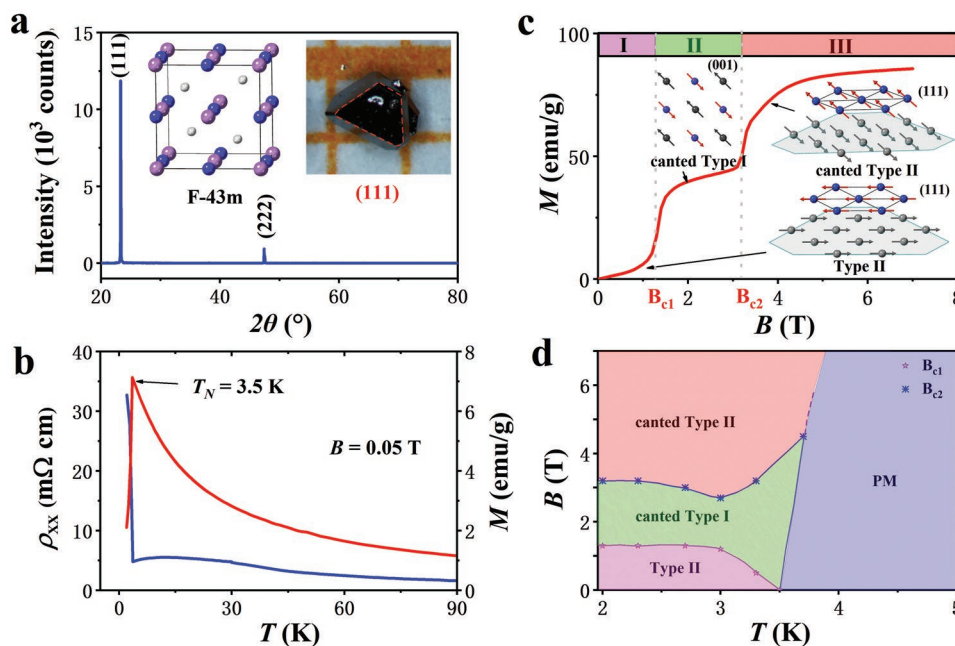

Figure 1. Crystal structure and metamagnetic transition in DyPtBi single crystal. a) The X-ray diffraction of single crystal. The insets show the crystal structure and a typical photograph of DyPtBi single crystal with the (111) plane. b) Temperature dependence of magnetization under $B = 0.05$ T with $B\,//\,[111]$ and resistivity under zero field and current $I\,//\,[1\text{-}10]$. c) Isothermal magnetization curve of DyPtBi single crystal with B // [1-10] and T = 2 K. The entire magnetization process is divided into three parts, and the insets show the corresponding antiferromagnetic structures. d) Phase diagram of the magnetic structure under an external magnetic field up to 7 T.
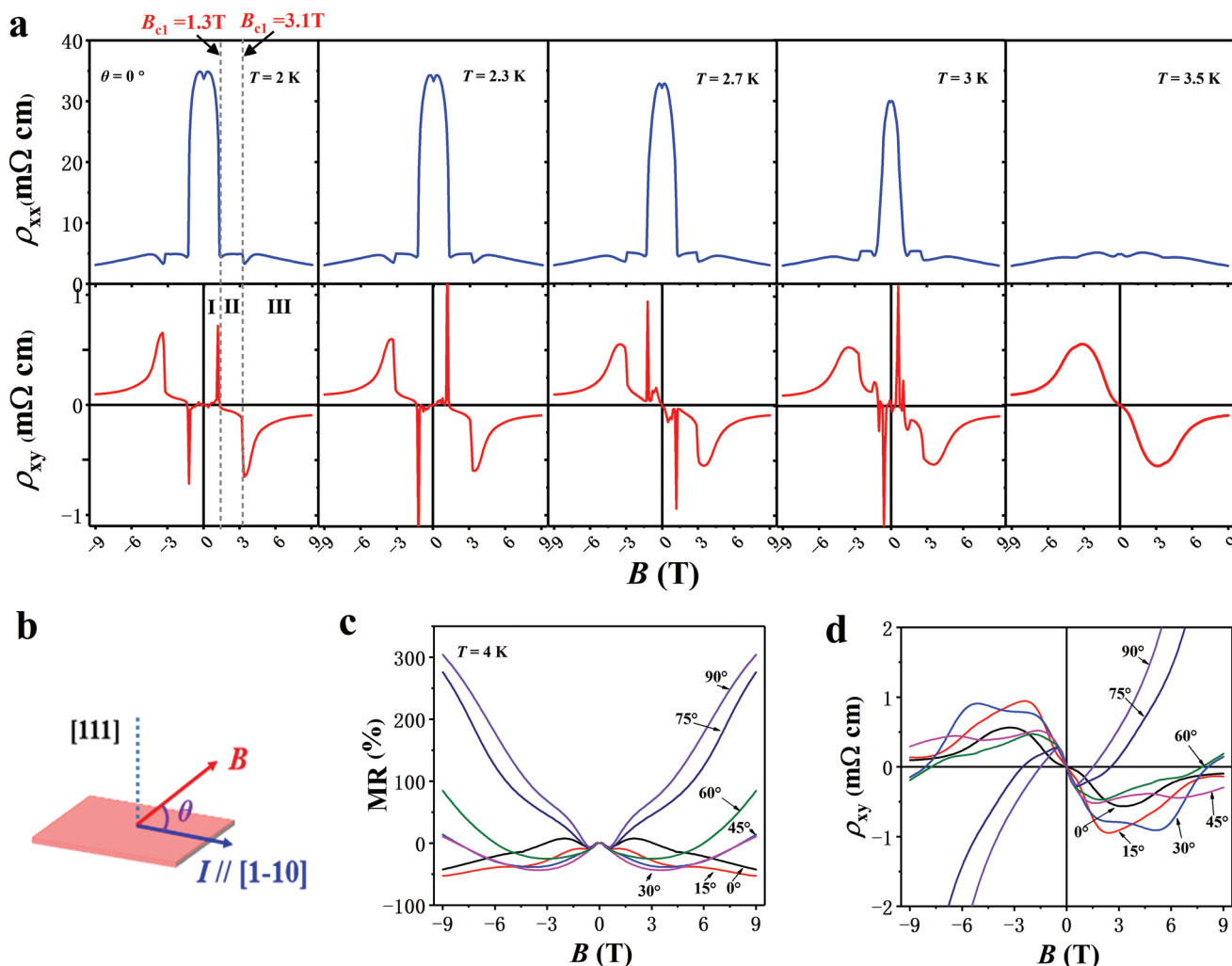
Figure 2. Temperature dependence of the Hall resistivity with $\theta = 0°$ and angular θ dependence of the MR and Hall resistivity at $T = 4$ K. a) The MR and Hall resistivity curves with $\theta = 0°$ and $T \leq T_N$. The dash lines are critical magnetic fields of metamagnetic transitions. b) Configuration of the magnetic field and current in the out-of-plane measurement, where θ is the angle between B and I. (c) and (d) angular θ dependence of MR and Hall resistivity at $T = 4$ K.

semimetals, and topological insulators.[15] Therefore, the change in magnetic symmetries in the metamagnetic transition will strongly modulate the topological band and topological physical properties, such as the unconventional Hall effect related to the net Berry curvature.

2.2. Unconventional Hall Resistivity below and above T_N at $\theta = 0°$

To further characterize the transport properties, we measured the temperature dependence of longitudinal resistivity $\rho_{xx}(B)$ and Hall resistivity $\rho_{xy}(B)$ from 2 to 3.5 K (T_N) with $\theta = 0°$ (magnetic field nominally parallel to the current), as shown in **Figure 2**a. Materials with metamagnetic transitions usually exhibit complex Hall behavior that makes the extraction progress difficult.[5b,10c] Ideally, the normal Hall signal should be zero when magnetic field is collinear with the current. There-

fore, the measurement with $\theta = 0°$ should contain a smaller normal Hall contribution. Because of the strong coupling between conduction electrons and the localized 4f moment of Dy, longitudinal resistivity $\rho_{xx}(B)$ also shows a strong coupling to the magnetic phase. At $T < T_N$, $\rho_{xx}(B)$ sharply decreases across the lower critical magnetic field (B_{c1}) and the large negative MR reaches −80% at 2 K in region I. Rotating B from out-of-plane to in-of-plane, the large MR is almost unchanged (see Figure S7d, Supporting Information) and the negative MR does not depend on the direction of the applied field. This also indicates that the negative MR does not share the same origin as the negative MR induced by chiral anomaly. $\rho_{xy}(B)$ is almost zero in the type II states, which is consistent with the fact that the collinear AFM state does not have a net Berry curvature. With increasing T, $\rho_{xy}(B)$ in the type II state shows complex behavior. It may be coming from the coupling effect between conduction electrons and the localized 4f moment of Dy. However, a sharp jump is exhibited at critical point B_{c1}, which may be related to

ADVANCED
SCIENCE NEWS
www.advancedsciencenews.com

ADVANCED
FUNCTIONAL
MATERIALS
www.afm-journal.de

the intermediate state of the spin texture and requires further study to clarify the origin. With increasing B, a small Hall signal with a negative slope is observed in region II. The magnetization curve in Figure 1c reveals that the canted type I state shows a fixed net magnetic moment in the material and it breaks the collinear AFM structure and changes symmetries of the AFM state. Therefore, the small signal may come from a net Berry curvature, analogous to other non-collinear AFM materials, such as Mn_3Sn and Mn_3Ge.[16] $\rho_{xx}(B)$ in this region slightly increases. Interestingly, with the change in the symmetry of magnetic structure (from canted type I to canted type II), a large unconventional Hall signal is observed in region III. The large difference indicates that the structure of the canted AFM may have a large influence on the band structure and corresponding AHE. The ρ_{xy} hump in region III shows an abrupt jump at B_{c2} and followed by a smooth decrease with increasing B. ρ_{xx} shows a dip at B_{c2} and a decrease in region III. By comparing the Hall signals of these three regions, we know that canted spin texture is a key factor in observing the unconventional Hall signal and that the symmetry of spin texture will strong influence the AHE. At $T < T_N$, the critical field of the hump decreases with increasing T and disappears at T_N. The hump becomes wide and smooth as T approaching to T_N. The smooth transition in this process indicates that the unconventional Hall signal can retain to above T_N (paramagnetic state), and the signals share the same origin of below and above T_N. $EuCd_2As_2$ is another material that exhibits an unconventional AHE both above and below the magnetic transition temperature[5a] and was identified as being in a spin-fluctuation-induced WSM state in paramagnetic phase by angle-resolved photoemission spectroscopy (ARPES) measurements.[7b] The large negative MR in region I slowly decreases in magnetic order and disappears at T_N.

2.3. Chiral Anomaly and Angular Dependence of the Hall Resistivity

RPtBi compounds were predicted to be topological materials, including topological insulators[8a,b] and magnetic-field-induced WSMs.[9b,17] In addition to the indication of a negative MR in region III, these remind us that the chiral anomaly may also exist in DyPtBi single crystal. Because the large negative MR at $T < T_N$ will strongly influence the observation of the chiral anomaly. Here, we choose longitudinal resistivity at 4 K ($T > T_N$) with I // [1-10] and B rotating in the out-of-plane to study the chiral-anomaly-induced negative MR (Figure 2b). The MR exhibits a large positive value of 300% at 9 T when the magnetic field is perpendicular to the plane of current ($\theta = 90°$). When B rotates towards the I direction, the MR value decrease and becomes negative when $\theta \leq 60°$. The maximum negative value is -60% (Figure S3, Supporting Information), larger than that of HoPtBi and lower than that of TbPtBi, which is consistent with the principle of RPtBi.[18] The evolution of the Hall resistivity under the rotating the magnetic field is consistent with that of MR. As shown in Figure 2c, $\rho_{xy}(B)$ first decreases and then changes the sign and forms a hump in low magnetic fields at $\theta \leq 60°$. The normal Hall resistivity induced by the Lorentz force is with respect to the vertical component of B. However, the vertical component

of B maintains a positive value when B rotates from $\theta = 90°$ to $\theta \leq 60°$. Therefore, the sign change here means that there must be another contribution to the Hall resistivity and that the negative contribution is large enough to cover the normal Hall signal at $\theta \leq 60°$. $\rho_{xy}(B)$ shows two peaks at low B and high B. The two peaks increase as B rotates from $\theta = 60°$ to $\theta = 30°$. However, the feature of two peaks disappeared when $\theta \leq 15°$ and the peak at low magnetic fields is retained. It first increases with θ from 60° to 15° and then decreases as θ approaches zero. The normal Hall signal is small at $\theta \leq 15°$ and the unconventional Hall signal dominates the Hall resistivity. The complex Hall behavior implies strong anisotropy in DyPtBi. The temperature dependence of the negative MR and Hall resistivity with $\theta = 0°$ is shown in Figure S3, Supporting Information. The negative MR, suggestive of chiral anomaly originating from the Weyl points, gradually decreases with increasing temperature and persists to 50 K. The unconventional Hall resistivity shows a similar T-dependent behavior. In addition to the topological band nature, the close correlation between the negative MR and the unconventional Hall signal supports the Berry curvature mechanism as the origin of the unconventional AHE.

2.4. Detailed Out-of-Plane Unconventional Hall Resistivity

In this part, we focus on the unconventional Hall effect with B approaching to the current plane below and above T_N. The detailed measurement of the Hall resistivity with B approaching the current plane at 2 and 4 K are shown in **Figure 3**. Figure 3a shows the $\rho_{xy}(B)$ curves at $T = 2$ K ($< T_N$) and $-4° \leq \theta \leq 14°$. Obviously, $\rho_{xy}(B)$ in region III decreases with decreasing θ and almost disappears at $\theta = 5°$. A slight misalignment between B and the current plane appears in this measurement, and the magnetic field is not strictly parallel to the current at $\theta = 0°$. Similar behavior is also observed in the topological materials Mn_3Ge[16a] and $ZrTe_5$.[19] In a certain θ range, there is an obviously enhancement of the hump in region III. Figure 3b shows the angular dependence of the magnitude of the Hall resistivity. $\rho_{xy}(B)$ smoothly grows as B is tilted away from the current plane by a finite angle θ and approaches saturation at $\theta = 18°$ and $\theta = -10°$. $\rho_{xy}(B)$ reaches 0.89 mΩ cm. The close relation between the large $\rho_{xy}(B)$ hump in low magnetic fields and the direction of the applied field implies that the magnetic field is a controlling factor. Note that $\rho_{xy}(B)$ exhibits a slight dissymmetry between $\theta > 5°$ and $\theta < 5°$. This dissymmetry comes from the planar anisotropic anomalous Hall signal introduced by the misalignment of B and I in the plane (there is an angle between B and I in the current plane). This also means that the unconventional Hall resistivity has strong anisotropy in the plane. Figure 3c exhibits the $\rho_{xy}(B)$ curves at $T = 4$ K ($> T_N$) and $-10° \leq \theta \leq 18°$. When B is coplanar with current plane ($\theta = 5°$), the $\rho_{xy}(B)$ is nearly linear curves paralleling to $\rho_{xy}(B) = 0$. This means that the net magnetic moment following the external magnetic field lie in the current plane. The angular-dependent properties of the large hump follow the same principle as that at 2 K. However, the dissymmetry between $\theta > 5°$ and $\theta < 5°$ become more obvious. These results indicate that the out-of-plane Hall resistivity shows a large anisotropy. Then,
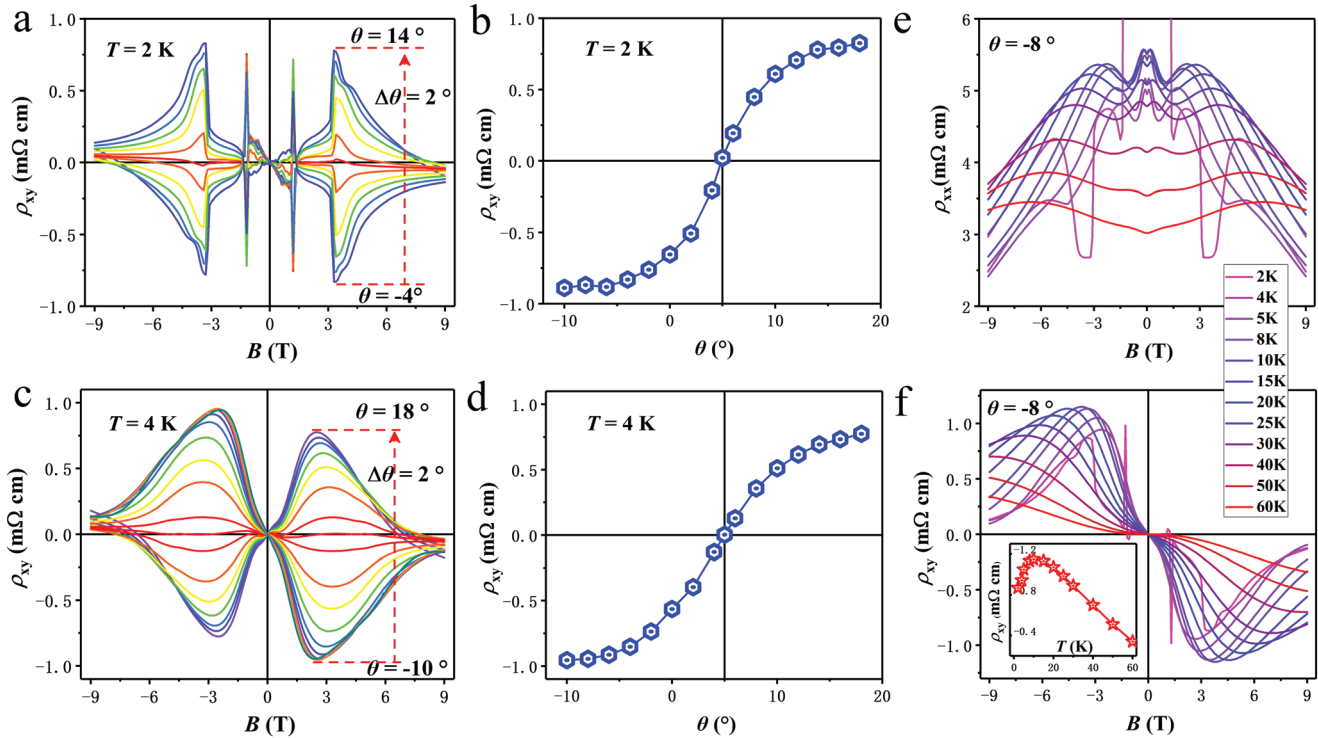
**ADVANCED
SCIENCE NEWS**

www.advancedsciencenews.com

**ADVANCED
FUNCTIONAL
MATERIALS**

www.afm-journal.de

Figure 3. Out-of-plane Hall resistivity at different angles θ and temperatures. a) Magnetic field dependence of Hall resistivity ρ_{xy} at $-4\,^\circ < \theta < 14\,^\circ$ and $T = 2$ K. b) Angular dependence of Hall resistivity ρ_{xy} obtained from the peak of the curves in (a). c) Magnetic field dependence of Hall resistivity ρ_{xy} at $-10\,^\circ < \theta < 18\,^\circ$ and $T = 2$ K. d) Angular dependence of Hall resistivity ρ_{xy} obtained from the peak of the curves in (c). (e) and (f) are MR and Hall resistivity at different temperatures and $\theta = -8\,^\circ$, respectively. The inset of (f) shows the temperature dependence of the Hall resistivity.

we measured the temperature dependence of the MR and Hall resistivity at a certain $\theta = -8°$. The chiral-anomaly-induced negative MR contribution maintains to 60 K in Figure 3e, which is similar to that of TbPtBi.[18] The anomalous Hall resistivity can also be observed at 60 K, which is much higher than $T_N = 3.5$ K. The close correlation between the negative MR and the unconventional Hall resistivity further supports the Weyl node origin of the AHE. The inset shows the temperature dependence of the $\rho_{xy}(B)$ curve. With increasing T, $\rho_{xy}(B)$ first increases and then decreases.

2.5. Planar AHE and Separation of the Normal and Anomalous Hall Resistivities

The configuration of the planar AHE measurement is exhibited in **Figure 4**a, B lies in the current plane, and ϕ is the angle between B and the normal line of the current direction. Figure 4b shows the planar Hall resistivity at $T = 4$ K and $B = 1$ T. In general, the Hall resistivity ρ_{xy} of magnetic materials can be expressed as $\rho_{xy} = \rho_{xy}^N + \rho_{xy}^A$, where $\rho_{xy}^N = R_H B$ is normal Hall resistivity and ρ_{xy}^A is the anomalous Hall resistivity. Here, B is perpendicular to the plane of the Hall voltage and current. ρ_{xy}^N should depend on the angle between B and I. Obviously, there are two different period signals when the magnetic field rotates in the current plane (see Figure 4b). The (111) plane has been identified XRD. The normal line of the (111) plane is a three-fold rotation axis. Therefore, the Hall signal with a period $2\pi/3$

should be crystal axis dependent. The Hall signal with a period 2π depends on the angle between B and I (actually, it depends on the vertical component of B). As we all known, the misalignment is inevitable in the actual planar measurement. The magnetic field is not strictly coplanar with current. Misalignment will introduce a normal Hall signal. Based on this fact, we further measured the planar Hall resistivity for different B and fit the curves with an equation form:

$$\rho_{xy} = A\cos(2\pi\varphi/3 + c) + B\cos(2\pi\varphi + d) \tag{1}$$

where $\rho_{xy}^A = A\cos(2\pi\varphi/3 + c)$ and $\rho_{xy}^N = A\cos(2\pi\varphi + d)$. The perfect fitting (red line) for the ρ_{xy}(1 T) in Figure 4b indicates that the two signals can be separated. Figure 4c shows the two separated signals, ρ_{xy}^A and ρ_{xy}^N. The oscillation amplitudes of ρ_{xy}^A and ρ_{xy}^N are $A(\rho_{xy}^A) = 0.58$ mΩ cm and $B = 0.18$ mΩ cm. The AHE contribution is much less sensitive to the tilt angle compared with the out-of-plane experiment. Figure 4d shows the magnetic field dependence of the Hall resistivity at $0° \le \phi \le 180°$. The remarkably large unconventional Hall signal at $\phi = 0°$ reaches 1.86 mΩ cm, which is approximately two times of the out-of-plane Hall resistivity. Interestingly, the sigh and magnitude of ρ_{xy} show two different periods. As Figures S4 and S5, Supporting Information, show, ρ_{xy} changes sign with a period $2\pi/3$. However, the magnitude of ρ_{xy} shows a half period with π (period: 2π). Obviously, the hump-like Hall signal has the same origin as the planar Hall resistivity with period $2\pi/3$. The amplitude of the planar Hall resistivity with period $2\pi/3$
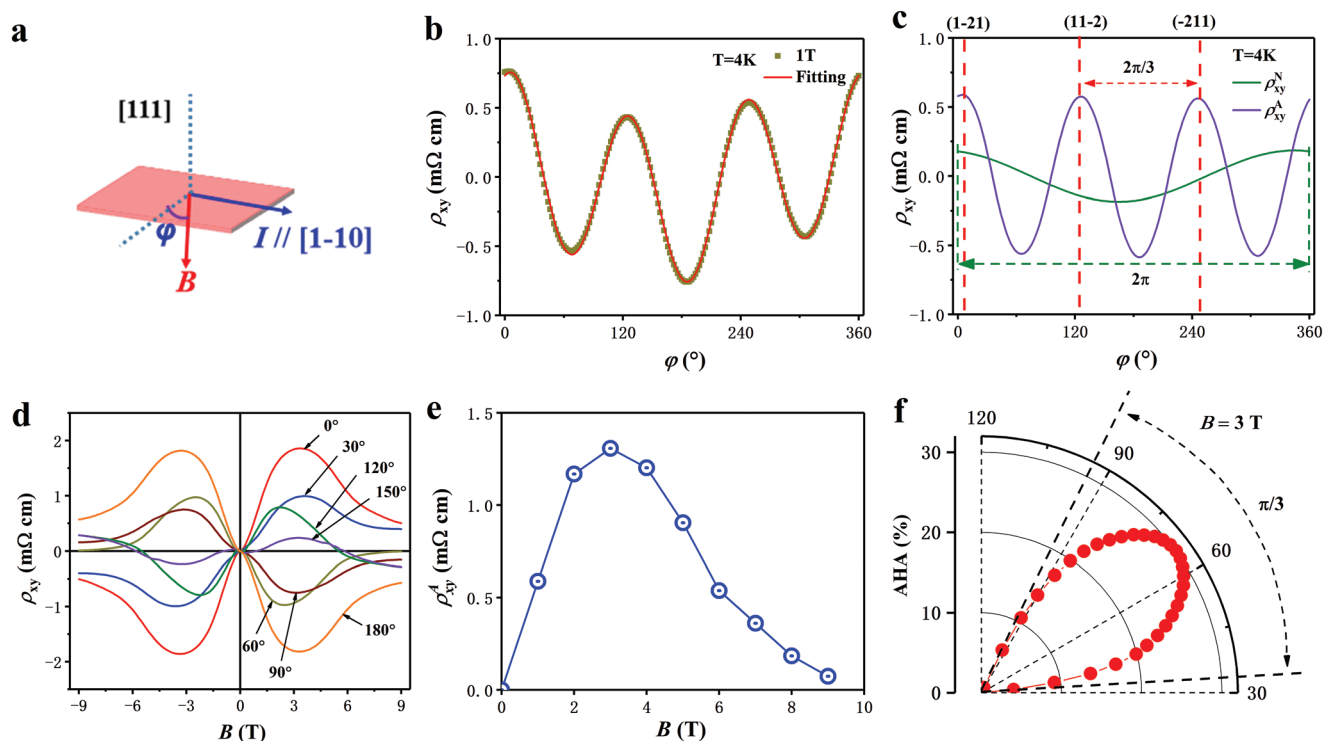
Figure 4. Planar Hall resistivity at 4K. a) Configuration of B and I in the in-plane Hall resistivity measurement. φ is defined as the angle between the magnetic field and the normal line of the current direction. b) Angular φ dependence of ρ_{xy} at $B = 1$ T. The red line is the fitting curve obtained by $\rho_{xy} = A\cos(a\phi + b) + B\cos(c\phi + d)$. The Hall signal can be divided into two cosine function signals with periods $2\pi/3$ and 2π. c) Normal Hall resistivity ρ_{xy}^N (cosine function signal with period 2π) and anomalous Hall resistivity ρ_{xy}^A (cosine functional signal with period $2\pi/3$) separated based on the fitting line at $T = 4$ K and $B = 1$ T. d) Magnetic field dependence of Hall resistivity ρ_{xy} at different angles φ. e) Magnetic field dependence of amplitude $A = \rho_{xy}^A$. f) Angular φ dependence of the AHA at 3 T.

was extracted by Equation (1) and is shown in Figure 4e. The peak reaches to $A = 1.31$ mΩ cm at 3 T. The hump-like curve confirms that the period of the unconventional anomalous Hall resistivity is $2\pi/3$ and is not related to the normal Hall resistivity. The unconventional anomalous Hall resistivity is strongly dependent on the crystal direction of the applied B. The AHA at $B = 3$ T reaches 30% as shown in Figure 4f. Combining the principles of the out-of-plane and in-of-plane Hall resistivity, we have reason to believe that a larger unconventional anomalous Hall signal and AHA will be got at certain θ and ϕ. These properties make DyPtBi compound a good platform to study giant AHA.

3. Discussion

Theoretically, RPtBi is predicted to be a topological insulator due to the HgTe-like crystal structure and band inversion.[8a] Combined with observations of chiral-anomaly-induced negative MR and two step-like metamagnetic transitions, DyPtBi has promise as be a good platform to study magnetism-driven multiple topological phase transition. As mentioned in the introduction, systems combining the topological bands and metamagnetic transitions are rare but exhibit plentiful topological phases and excellent physical properties. As a feature of the magnetic topological materials, the AHE related to the net Berry curvature usually reflects changes in topological properties. Therefore,

the magnetic structure dependence of the unconventional anomalous Hall resistivity in DyPtBi suggests that different topological states are induced by the strong coupling of magnetism and the electronic band. The typical magnetism-driven topological transition quantum materials, $MnBi_2Te_4$[20] and $EuCd_2As_2$,[5a] show several topological phases, that is, topological insulator, axion insulator, and WSM phases, and exhibit a magnetic structure dependence of the AHE.[5a,6b] Moreover, the process of the metamagnetic transition is usually a continuous process in certain magnetic phases. For instance, the canting angle of the canted AFM will continuous rotate with increasing B, and the AHE usually exhibits nonlinear behavior.[21] A nonlinear anomalous Hall resistivity and an anomalous Nernst effect have been observed in canted AFM WSM $EuCd_2As_2$ and attributed to the Weyl points near the Fermi level.[5a] The research on $EuTiO_3$ gives the detailed formation process of the nonlinear AHE and the corresponding band structure evolution.[5e] In these cases, a net Berry curvature in momentum space can be created in the canted AFM state. In addition to the Berry curvature mechanism, the nonlinear behavior of Hall resistivity also observed magnetic skyrmion lattice. For instance, in Gd_2PdSi_3[22] and $GdRu_2Si_2$,[23] a skyrmion lattice phase is sandwiched by two incommensurate spin-state phases and a nonlinear Hall resistivity is observed in this spin texture phase. The topological Hall effect induced by topological magnetic textures with a finite Berry curvature in real space will emerge when electron couple with the magnetic

moment.[22–24] In DyPtBi compound, the Ruderman–Kittel–Kasuya–Yosida (RKKY) type interaction among the local 4f moments dominates and show rich magnetic phases including modulated structures. Therefore, the real-space scenario for the unconventional Hall signal, as another possible source, should be considered in DyPtBi. However, the nonlinear behavior of DyPtBi was observed not only at the magnetic ordering temperature, but also in paramagnetic state that is much higher than T_N. The topological Hall effect can only exist at $T < T_N$.

Another feature is that the AHE emerges above and below the magnetic transition temperature. The temperature dependence of the Hall resistivity in Figure 2 implies that the unconventional Hall effect in these two T ranges has the same origin. The AHE has mostly been observed at magnetic ordering temperature. Therefore, the AHE in paramagnetic or nonmagnetic states has rarely been observed in several topological systems, for example ZrTe$_5$,[19a] EuCd$_2$As$_2$,[10c] and half-Heusler compounds.[9a,10b,17,25] The common feature of these materials is that the Weyl nodes are created by an external magnetic field. In particular, for AFM EuCd$_2$As$_2$, the existence of Weyl nodes in the paramagnetic state was identified by angle-resolved photoemission spectroscopy (ARPES) experiments and attributed to the interplay of itinerant electrons and localized moments.[7b] Based on the similar conditions of DyPtBi and EuCd$_2$As$_2$, spin fluctuation may induce Weyl points, and the Berry curvature mechanism related to Weyl points can explain the AHE in DyPtBi single crystal. All the results of DyPtBi support that the unconventional Hall resistivity originates from the Berry curvature mechanism and suggest that it hosts a magnetism-driven topological transition.

The planar AHE measurement indicate that the unconventional Hall signal shows a strong dependence on the crystal axis of the applied B, and the two signals, ρ_{xy}^A and ρ_{xy}^N were successful separated. The AHA of 30% reported here at $B = 3$ T is significant compared to, for example, the typical magnetic WSM Co$_3$Sn$_2$S$_2$ with AHA = 20%,[2d] Co$_2$MnAl with AHA = 22.5%,[2e] and MnGe thin film with Giant AHA, AHA = 18%.[26] This means that this compound could exhibit quantum AHE in the 2D limit state. Combining the canted type II spin texture and axis dependence, we can deduce that the AHE can be easily controlled by an external magnetic field. More tunable effects can be realized in this compound though the interplay between magnetism and the band structure.

4. Conclusion

To summarize, we observed a large unconventional AHE with B approaching to the current plane in the metamagnetic topological materials, DyPtBi single crystal. The abundant magnetic phase strongly influences the band structure and topological properties. Then, it further tunes the magnetotransport and induces a large unconventional Hall signal in region III. The evolution of this signal around the magnetic ordering temperature ($T_N = 3.5$ K) indicates the humps in region III below T_N and above T_N have the same source, which may be related to the topological band of DyPtBi. Our findings demonstrate that the band structure of DyPtBi is strongly coupled with the magnetic structure and that a net

Berry curvature in momentum space is created in the canted AFM state and paramagnetic state. The unconventional Hall signal shows a threefold rotation axis dependence when B rotates in the current plane (111) with a period of $2\pi/3$. Our results indicate that a higher AHA will be obtained when a 4π rotation measurement is carried out. DyPtBi is a good platform to study the unconventional AHE. Considering the great properties of DyPtBi compound, it is worthy of more attention to further research.

5. Experimental Section

Single Crystal Growth: High quality DyPtBi single crystals were grown by the Bi flux method.[13] For single crystal growth, a mixture of pure elements (molar ratio: Dy:Pt:Bi = 1:1:20) was prepared and placed in an alumina crucible. To prevent oxidation at high temperature, the whole tube was sealed in an evacuated quartz tube. Crystal growth process: first, the tube was heated from room temperature to 1150 °C and maintained at this temperature for 1 day, and then slowly cooled to 650 °C at a rate of 2 K h^{-1}. The excess Bi flux was removed by centrifuging the tube at 650 °C.

Physical Property Characterization: The magnetic properties were measured in a Quantum Design Magnetic Properties Measurement System (7 T, MPMS 3) and a Physical Property Measurement System (9 T, PPMS). The magnetotransport measurement was carried out based on the four-probe method in a Physical Property Measurement System (9 T, PPMS) with a sample rotator. The crystal structure of single crystals was characterized by a Rigaku XRD system with Cu K_α radiation ($\lambda = 1.5418$ Å) at room temperature.

Supporting Information

Supporting Information is available from the Wiley Online Library or from the author.

Conflict of Interest

The authors declare no conflict of interest.

Data Availability Statement

Research data are not shared.

[1] a) A. Sakai, Y. P. Mizuta, A. A. Nugroho, R. Sihombing, T. Koretsune, M.-T. Suzuki, N. Takemori, R. Ishii, D. Nishio-Hamane, R. Arita, P. Goswami, S. Nakatsuji, *Nat. Phys.* **2018**, *14*, 1119. b) S. N. Guin, K. Manna, J. Noky, S. J. Watzman, C. Fu, N. Kumar, W. Schnelle, C. Shekhar, Y. Sun, J. Gooth, C. Felser, *NPG Asia Mater.* **2019**, *11*, 16.

[2] a) C.-Z. Chang, J. Zhang, X. Feng, J. Shen, Z. Zhang, M. Guo, K. Li, Y. Ou, P. Wei, L.-L. Wang, Z.-Q. Ji, Y. Feng, S. Ji, X. Chen, J. Jia, X. Dai, Z. Fang, S.-C. Zhang, K. He, Y. Wang, L. Lu, X.-C. Ma, Q.-K. Xue, *Science* **2013**, *340*, 167. b) Y. F. Zhao, R. Zhang, R. Mei, L. J. Zhou, H. Yi, Y. Q. Zhang, J. Yu, R. Xiao, K. Wang, N. Samarth, M. H. W. Chan, C. X. Liu, C. Z. Chang, *Nature* **2020**, *588*, 419. c) E. D. L. Rienks, S. Wimmer, J. Sanchez-Barriga, O. Caha, P. S. Mandal, J. Ruzicka, A. Ney, H. Steiner, V. V. Volobuev, H. Groiss, M. Albu, G. Kothleitner, J. Michalicka, S. A. Khan, J. Minar, H. Ebert, G. Bauer, F. Freyse, A. Varykhalov, O. Rader, G. Springholz, *Nature* **2019**, *576*, 423. d) E. Liu, Y. Sun, N. Kumar, L. Muechler, A. Sun, L. Jiao, S.-Y. Yang, D. Liu, A. Liang, Q. Xu, J. Kroder, V. Süß, H. Borrmann, C. Shekhar, Z. Wang, C. Xi, W. Wang, W. Schnelle, S. Wirth, Y. Chen, S. T. B. Goennenwein, C. Felser, *Nat. Phys.* **2018**, *14*, 1125. e) P. Li, J. Koo, W. Ning, J. Li, L. Miao, L. Min, Y. Zhu, Y. Wang, N. Alem, C. X. Liu, Z. Mao, B. Yan, *Nat. Commun.* **2020**, *11*, 3476. f) K. Kim, J. Seo, E. Lee, K. T. Ko, B. S. Kim, B. G. Jang, J. M. Ok, J. Lee, Y. J. Jo, W. Kang, J. H. Shim, C. Kim, H. W. Yeom, B. Il Min, B. J. Yang, J. S. Kim, *Nat. Mater.* **2018**, *17*, 794.

[3] a) C. Liu, Y. Wang, H. Li, Y. Wu, Y. Li, J. Li, K. He, Y. Xu, J. Zhang, Y. Wang, *Nat. Mater.* **2020**, *19*, 522. b) P. Wei, J. S. Moodera, *Nat. Mater.* **2020**, *19*, 481.

[4] M. A. Wilde, M. Dodenhöft, A. Niedermayr, A. Bauer, M. M. Hirschmann, K. Alpin, A. P. Schnyder, C. Pfleiderer, *Nature* **2021**, *594*, 374.

[5] a) Y. Xu, L. Das, J. Z. Ma, C. J. Yi, S. M. Nie, Y. G. Shi, A. Tiwari, S. S. Tsirkin, T. Neupert, M. Medarde, M. Shi, J. Chang, T. Shang, *Phys. Rev. Lett.* **2021**, *126*, 076602. b) S. S. Sunku, T. Kong, T. Ito, P. C. Canfield, B. S. Shastry, P. Sengupta, C. Panagopoulos, *Phys. Rev. B* **2016**, *93*, 174408. c) T. Asaba, Y. Su, M. Janoschek, J. D. Thompson, S. M. Thomas, E. D. Bauer, S.-Z. Lin, F. Ronning, *Phys. Rev. B* **2020**, *102*, 035127. d) K. Ueda, R. Kaneko, H. Ishizuka, J. Fujioka, N. Nagaosa, Y. Tokura, *Nat. Commun.* **2018**, *9*, 3032. e) K. S. Takahashi, H. Ishizuka, T. Murata, Q. Y. Wang, Y. Tokura, N. Nagaosa, M. Kawasaki, *Sci. Adv.* **2018**, *4*, eaar7880.

[6] a) J. Cui, M. Shi, H. Wang, F. Yu, T. Wu, X. Luo, J. Ying, X. Chen, *Phys. Rev. B* **2019**, *99*, 155125. b) S. H. Lee, Y. Zhu, Y. Wang, L. Miao, T. Pillsbury, H. Yi, S. Kempinger, J. Hu, C. A. Heikes, P. Quarterman, W. Ratcliff, J. A. Borchers, H. Zhang, X. Ke, D. Graf, N. Alem, C.-Z. Chang, N. Samarth, Z. Mao, *Phys. Rev. Res.* **2019**, *1*, 012011.

[7] a) J. Ma, H. Wang, S. Nie, C. Yi, Y. Xu, H. Li, J. Jandke, W. Wulfhekel, Y. Huang, D. West, P. Richard, A. Chikina, V. N. Strocov, J. Mesot, H. Weng, S. Zhang, Y. Shi, T. Qian, M. Shi, H. Ding, *Adv. Mater.* **2020**, *32*, 1907565. b) J.-Z. Ma, S. M. Nie, C. J. Yi, J. Jandke, T. Shang, M. Y. Yao, M. Naamneh, L. Q. Yan, Y. Sun, A. Chikina, V. N. Strocov, M. Medarde, M. Song, Y.-M. Xiong, G. Xu, W. W. , J. Mesot, M. Reticcioli, C. Franchini, C. Mudry, M. Müller, Y. G. Shi, T. Qian, H. Ding, M. Shi, *Sci. Adv.* **2019**, *5*, eaaw4718.

[8] a) S. Chadov, X. Qi, J. Kubler, G. H. Fecher, C. Felser, S. C. Zhang, *Nat. Mater.* **2010**, *9*, 541. b) H. Lin, L. A. Wray, Y. Xia, S. Xu, S. Jia, R. J. Cava, A. Bansil, M. Z. Hasan, *Nat. Mater.* **2010**, *9*, 546. c) Z. K. Liu, L. X. Yang, S. C. Wu, C. Shekhar, J. Jiang, H. F. Yang, Y. Zhang, S. K. Mo, Z. Hussain, B. Yan, C. Felser, Y. L. Chen, *Nat. Commun.* **2016**, *7*, 12924.

[9] a) T. Suzuki, R. Chisnell, A. Devarakonda, Y. T. Liu, W. Feng, D. Xiao, J. W. Lynn, J. G. Checkelsky, *Nat. Phys.* **2016**, *12*, 1119. b) M. Hirschberger, S. Kushwaha, Z. Wang, Q. Gibson, S. Liang, C. A. Belvin, B. A. Bernevig, R. J. Cava, N. P. Ong, *Nat. Mater.*

[10] a) C. Y. Guo, F. Wu, Z. Z. Wu, M. Smidman, C. Cao, A. Bostwick, C. Jozwiak, E. Rotenberg, Y. Liu, F. Steglich, H. Q. Yuan, *Nat. Commun.* **2018**, *9*, 4622. b) J. Chen, H. Li, B. Ding, H. Zhang, E. Liu, W. Wang, *Appl. Phys. Lett.* **2021**, *118*, 031901. c) H. Zhang, Y. L. Zhu, Y. Qiu, W. Tian, H. B. Cao, Z. Q. Mao, X. Ke, *Phys. Rev. B* **2020**, *102*, 094424.

[11] E. Mun, S. L. Bud'ko, P. C. Canfield, *Phys. Rev. B* **2016**, *93*, 115134.

[12] C. Liu, Y. Lee, T. Kondo, E. D. Mun, M. Caudle, B. N. Harmon, S. L. Bud'ko, P. C. Canfield, A. Kaminski, *Phys. Rev. B* **2011**, *83*, 205133.

[13] J. Chen, H. Li, B. Ding, Z. Hou, E. Liu, X. Xi, G. Wu, W. Wang, *Appl. Phys. Lett.* **2020**, *116*, 101902.

[14] a) C. Hu, K. N. Gordon, P. Liu, J. Liu, X. Zhou, P. Hao, D. Narayan, E. Emmanouilidou, H. Sun, Y. Liu, H. Brawer, A. P. Ramirez, L. Ding, H. Cao, Q. Liu, D. Dessau, N. Ni, *Nat. Commun.* **2020**, *11*, 97. b) M. M. Otrokov, I. I. Klimovskikh, H. Bentmann, D. Estyunin, A. Zeugner, Z. S. Aliev, S. Gass, A. U. B. Wolter, A. V. Koroleva, A. M. Shikin, M. Blanco-Rey, M. Hoffmann, I. P. Rusinov, A. Y. Vyazovskaya, S. V. Eremeev, Y. M. Koroteev, V. M. Kuznetsov, F. Freyse, J. Sanchez-Barriga, I. R. Amiraslanov, M. B. Babanly, N. T. Mamedov, N. A. Abdullayev, V. N. Zverev, A. Alfonsov, V. Kataev, B. Buchner, E. F. Schwier, S. Kumar, A. Kimura, et al., *Nature* **2019**, *576*, 416. c) B. Chen, F. Fei, D. Zhang, B. Zhang, W. Liu, S. Zhang, P. Wang, B. Wei, Y. Zhang, Z. Zuo, J. Guo, Q. Liu, Z. Wang, X. Wu, J. Zong, X. Xie, W. Chen, Z. Sun, S. Wang, Y. Zhang, M. Zhang, X. Wang, F. Song, H. Zhang, D. Shen, B. Wang, *Nat. Commun.* **2019**, *10*, 4469.

[15] S. Nie, Y. Sun, F. B. Prinz, Z. Wang, H. Weng, Z. Fang, X. Dai, *Phys. Rev. Lett.* **2020**, *124*, 076403.

[16] a) A. K. Nayak, J. E. Fischer, Y. Sun, B. Yan, J. Karel, A. C. Komarek, C. Shekhar, N. Kumar, W. Schnelle, J. Kübler, C. Felser, S. S. P. Parkin, *Sci. Adv.* **2016**, *2*, e1501870. b) S. Nakatsuji, N. Kiyohara, T. Higo, *Nature* **2015**, *527*, 212.

[17] C. Shekhar, N. Kumar, V. Grinenko, S. Singh, R. Sarkar, H. Luetkens, S.-C. Wu, Y. Zhang, A. C. Komarek, E. Kampert, Y. Skourski, J. Wosnitza, W. Schnelle, A. McCollam, U. Zeitler, J. Kübler, B. Yan, H.-H. Klauss, S. S. P. Parkin, C. Felser, *Proc. Natl. Acad. Sci. USA* **2018**, *115*, 9140.

[18] J. Chen, H. Li, B. Ding, E. Liu, Y. Yao, G. Wu, W. Wang, *Appl. Phys. Lett.* **2020**, *116*, 222403.

[19] a) T. Liang, J. Lin, Q. Gibson, S. Kushwaha, M. Liu, W. Wang, H. Xiong, J. A. Sobota, M. Hashimoto, P. S. Kirchmann, Z.-X. Shen, R. J. Cava, N. P. Ong, *Nat. Phys.* **2018**, *14*, 451. b) J. Ge, D. Ma, Y. Liu, H. Wang, Y. Li, J. Luo, T. Luo, Y. Xing, J. Yan, D. Mandrus, H. Liu, X. C. Xie, J. Wang, *Natl. Sci. Rev.* **2020**, *7*, 1879.

[20] D. Zhang, M. Shi, T. Zhu, D. Xing, H. Zhang, J. Wang, *Phys. Rev. Lett.* **2019**, *122*, 206401.

[21] C. Le, C. Felser, Y. Sun, *arXiv* **2021**, 2105.09237v1.

[22] T. Kurumaji, T. Nakajima, Sagayama, H. N. , M. Hirschberger, Y. Taguchi, A. Kikkawa, T.-h. Arima, Y. Yamasaki, H. Sagayama, H. Nakao, Y. Taguchi, T.-h. Arima, Y. Tokura, *Science* **2019**, *365*, 914.

[23] N. D. Khanh, T. Nakajima, X. Yu, S. Gao, K. Shibata, M. Hirschberger, Y. Yamasaki, H. Sagayama, H. Nakao, L. Peng, K. Nakajima, R. Takagi, T. H. Arima, Y. Tokura, S. Seki, *Nat. Nanotechnol.* **2020**, *15*, 444.

[24] T. Shang, Y. Xu, D. J. Gawryluk, J. Z. Ma, T. Shiroka, M. Shi, E. Pomjakushina, *Phys. Rev. B* **2021**, *103*, L020405.

[25] Y. Zhu, B. Singh, Y. Wang, C.-Y. Huang, W.-C. Chiu, B. Wang, D. Graf, Y. Zhang, H. Lin, J. Sun, A. Bansil, Z. Mao, *Phys. Rev. B* **2020**, *101*, 161105.

[26] Y. Fujishiro, N. Kanazawa, R. Kurihara, H. Ishizuka, T. Hori, F. S. Yasin, X. Yu, A. Tsukazaki, M. Ichikawa, M. Kawasaki, N. Nagaosa, M. Tokunaga, Y. Tokura, *Nat. Commun.* **2021**, *12*, 317.